Journal of Power Sources 184 (2008) 265–275

Contents lists available at ScienceDirect

Journal of Power Sources

journal homepage: www.elsevier.com/locate/jpowsour

# $H_2$ production from $CH_4$ decomposition: Regeneration capability and performance of nickel and rhodium oxide catalysts

M.E. Rivas[a], C.E. Hori[b], J.L.G. Fierro[a,*], M.R. Goldwasser[c], A. Griboval-Constant[d]

[a] Instituto de Catálisis y Petroleoquímica, CSIC, Marie Curie n° 2, Cantoblanco, 28049 Madrid, Spain
[b] Faculdade de Engenharia Química, Universidade Federal de Uberlândia, Av. João Naves de Ávila 2121, Campus Santa Mônica, Bloco 1K, 38400-902 Uberlândia, MG, Brazil
[c] Centro de Catálisis Petróleo y Petroquímica, Escuela de Química, Facultad de Ciencias, Universidad Central de Venezuela, Apartado 47102, Los Chaguaramos, Caracas, Venezuela
[d] Unité de Catalyse et Chimie du Solide, UMR CNRS 8181, U.S.T.L., Bâtiment C3, 59655, Villeneuve D'Ascq, Cedex, France

ARTICLE INFO

*Article history:*
Received 13 March 2008
Received in revised form 3 June 2008
Accepted 4 June 2008
Available online 8 June 2008

*Keywords:*
Ni–Rh perovskite precursors
Methane decomposition
Hydrogen production
Characterization of catalysts

ABSTRACT

Nickel–lanthanum ($LaNiO_3$) and nickel–rhodium–lanthanum ($LaNi_{0.95}Rh_{0.05}O_3$) perovskite-type oxide precursors were synthesized by different methodologies (co-precipitation, sol–gel and impregnation). They were reduced in an $H_2$ atmosphere to produce nickel and rhodium nanoparticles on the $La_2O_3$ substrate. All samples were tested in the catalytic decomposition of $CH_4$. Methane decomposed into carbon and $H_2$ at reaction temperatures as low as 450 °C—no other reaction products were observed. Conversions were in the range of 14–28%, and $LaNi_{0.95}Rh_{0.05}O_3$ synthesized by co-precipitation was the most active catalyst. All catalysts maintained sustained activity even after massive carbon deposition indicating that these deposits are of the nanotube-type, as confirmed by transmission electron microscopy (TEM). The reaction seems to occur in a way that a nickel or rhodium crystal face is always clean enough to expose sufficient active sites to make the catalytic process continue. The samples were subjected to a reduction–oxidation–reduction cycle and *in situ* analyses confirmed the stability of the perovskite structure. All diffraction patterns showed a phase change around 400 °C, due to reduction of $LaNiO_3$ to an intermediate $La_2Ni_2O_5$ structure. When the reduction temperatures reach 600 °C, this structure collapses through the formation of $Ni^0$ crystallites deposited on the $La_2O_3$. Under oxidative conditions, the perovskite system is recomposed with nickel re-entering the $LaNiO_3$ framework structure accounting for the regenerative capability of these solids.



## 1. Introduction

The catalytic decomposition of methane (CDM) shows a promising alternative to the traditional methods of hydrogen production, such as methane steam reforming (MSR) and partial oxidation of methane (POM) [1,2]. Due to the absence of oxygen, the formation of carbon oxides is completely prevented in this process, and the need for additional downstream reactions, such as water–gas shift and selective oxidation, is eliminated. Moreover, the mixture of hydrogen and methane obtained from the CDM process could be directly used to feed internal combustion engines or gas turbine power plants [3], thus lowering the hydrogen production costs. Methane decomposition is a moderately endothermic process that requires 45.1 kJ mol$^{-1}$ of $H_2$ produced at 800 °C [4].

$$CH_4 \rightarrow C + 2H_2 \qquad \Delta H_{800\,^\circ C} = +90.1\ \text{kJ mol}^{-1} \tag{1}$$

Besides hydrogen, a CDM process also yields deposited carbon. The process requires not only a metal catalyst (Ni, Co, Fe and Pt) able to break the C–H bonds of the methane molecule, but also one that is able to maintain a high and sustained activity for a long time. On nickel catalysts, the carbon is usually deposited as nanofibers, which have several potential applications, such as electronic components, polymer additives, catalyst or catalyst support. In addition, this kind of carbon allows the catalyst to maintain its activity for an extended period of time without deactivation. Nickel is considered to be the most efficient metal, since it catalyzes the decomposition of methane forming carbon nanofibers under relative mild conditions [5–8]. The stability and activity of Ni catalysts for CDM reaction depend on its textural properties and surface structure. A review of the results reported in literature shows that the morphological appearance of the deposited carbon and the kinetics of CDM are affected by the nature of the active sites of the catalyst [9], the structure of the catalytic system, the textural properties and the size of the catalyst particles [10], the nature of the support [11,12], and the operating conditions, including the concentration of methane in the feed [13] and the reactor flow rate [14]. CDM reaction needs

* Corresponding author. Tel.: +34 91 585 4769; fax: +34 91 585 4767.
*E-mail address:* jlgfierro@icp.csic.es (J.L.G. Fierro).

0378-7753/$ – see front matter © 2008 Elsevier B.V. All rights reserved.
doi:10.1016/j.jpowsour.2008.06.002

Ni-catalysts in which Ni crystallites have been stabilized, in order to avoid sintering during the regeneration process.

An alternative option for stabilizing active metal particles is to use perovskite-type oxides as precursors. Thus, these materials appear as potential candidates to catalyze the $CO_x$-free production of hydrogen from methane decomposition. Perovskite-type oxides of general formula $ABO_3$ (A: alkaline earth or lanthanide; B: transition element) are highly stable under the severe conditions, such as high temperature, imposed by these reactions. In these materials, A is a large cation, responsible for the thermal resistance, and B is a redox cation, responsible for catalytic activity. When subjected to reduction processes, perovskite-type oxides produce very small particles, in the order of nanometers, with high metallic dispersion [15,16]. The efficient use of these catalyst precursors requires a high dispersion of the metal phase, which can be achieved by controlled segregation of the active phase. In addition, the flexibility of structure composition allows the preparation of bimetallic catalysts with different compositions and oxidation states. This may lead to structural defects that are highly appropriate to use in catalytic processes. Noble metals such as Ru, Rh, Pt and Ir are known to prevent the accumulation of coke on the catalyst surface during methane conversion reactions. Rh seems to be the metal that better fulfils this requirement with some compromise between activity and stability [17]. It is also well established that the synthesis method plays an important role in the catalytic performance for methane decomposition. The different synthesis methods generate structural, surface and textural changes in the properties of the materials, influencing their catalytic behavior [18].

In this work, we studied the catalytic performance and the regeneration capabilities of catalysts obtained from nickel and nickel–rhodium perovskite-type oxide precursors, synthesized by different methodologies (co-precipitation, sol–gel and impregnation), in the catalytic decomposition of methane.

## 2. Experimental

### 2.1. Catalyst preparation

Nickel–lanthanum ($LaNiO_3$) and nickel–rhodium–lanthanum ($LaNi_{0.95}Rh_{0.05}O_3$) perovskite-type oxides were synthesized according to the modified citrate [19] and co-precipitation [20] methods. They are referred, according to the synthesis method used, as $LaNi_{0.95}Rh_{0.05}O_3$-sg and $LaNiO_3$-sg when synthesized by sol–gel, $LaNi_{0.95}Rh_{0.05}O_3$-cp and $LaNiO_3$-cp synthesized by co-precipitation and $LaNiO_3$-imp synthesized by impregnation.

For the synthesis of sol–gel precursors, stoichiometric amounts of $La(NO_3)_3{\cdot}xH_2O$ (Merck, reagent grade) of $Ni(NO_3)_3{\cdot}6H_2O$ and $RhCl_3{\cdot}xH_2O$ (Merck, reagent grade) were dissolved in distilled water and then added to a second solution containing equimolecular amounts of citric (99.5, Riedel-de Haën) and ethylenglycol (99.5%, Riedel-de Haën) as a polydentate ligand. The excess of water was slowly removed in a rotary-evaporator until a viscous liquid was obtained. Then, it was slowly heated in air at a rate of 1 °C min$^{-1}$ from ambient temperature to 750 °C, and this temperature was kept for 5 h. These conditions are essential to obtain a crystalline material. Co-precipitated precursors of catalysts were prepared by the simultaneous precipitation of nickel and lanthanum ions using a solution of nitrate of nickel, nitrate of lanthanum, $RhCl_3{\cdot}xH_2O$ and $K_2CO_3$ as precipitating agent. La and Ni salt nitrates and Rh chloride salt were dissolved in distilled water to obtain 1 M solutions. Both solutions were mixed together under vigorous stirring. Then, a stoichiometric quantity plus 10% of an aqueous solution of $K_2CO_3$ (99.0% minimum, Johnson Matthey) was rapidly added. Under basic (pH > 9) conditions, water was partially evaporated by heating the solution to 70 °C. Before filtering, the precipitate was washed with ice-cooled distilled water until the pH of the filtrate became neutral. The precursors were then dried at 100 °C for 4 h and calcined at 750 °C for 5 h.

A reference $LaNiO_3$ supported material was synthesized by impregnation of $La_2O_3$ previously calcined by an aqueous solution of nickel nitrate. The excess of water was slowly removed in a rotary-evaporator and then the solid was calcined at 500 °C for 5 h.

### 2.2. Characterization

The chemical compositions of the catalyst precursors were analyzed by Inductively Coupled Plasma Emissions Spectroscopy (ICP) using a PerkinElmer ICP/5500 instrument. The structural characterization of all calcined catalyst precursors and spent catalysts were performed by powder X-ray diffraction with nickel-filtered Cu Kα radiation (λ = 0.1538 nm) using a Seifert 3000P instrument. XRD profiles were collected in the $2\theta$ range of 5–80°, in steps of 2° min$^{-1}$. Phase identification was carried out by comparison with the JCPDF database cards. Particle size of nickel crystallites were determined by the Scherrer equation using the Ni(1 1 1) reflection at $2\theta = 44.5°$ for line broadening measurements. BET specific surfaces areas were calculated from the nitrogen adsorption isotherms at liquid nitrogen temperature on a Micromeritics ASAP 2100 apparatus, taking a value of 0.162 nm$^2$ for the cross-sectional area of the adsorbed $N_2$ molecule. Prior to adsorption measurements, samples were degassed at 250 °C.

The reduction behavior of the oxides was studied by temperature-programmed reduction (TPR). The experiments were carried out on a semiautomatic Micromeritics TPD/TPR 2900 apparatus interfaced with a microcomputer. 20 mg of the sample was placed in a U-shaped quartz tube. The sample was first purged in a helium stream at 150 °C for 1 h and then cooled to room temperature. Reduction profiles were recorded by passing a 10% $H_2$/Ar flow at a rate of 50 mL min$^{-1}$ and heating rate of 10 °C min$^{-1}$ from room temperature to 800 °C. A cold-trap was placed just before the TCD of the instrument to remove the water from the exit stream.

Surface analyses for calcined and activated oxide precursors were carried out in a VG Escalab 200R electron spectrometer provided with Al Kα ($h\nu$ = 1486.6 eV, 1 eV = 1.6302 × 10$^{-19}$ J) X-ray source and a hemi-spherical electron analyzer. The powder samples, pressed in 8 mm diameter copper troughs, were fixed on the XYZ manipulator. The base pressure in the analysis chamber was maintained below 4 × 10$^{-9}$ mbar during data acquisition. The pass energy of the analyzer was set at 50 eV, for which the resolution as measured by the full width at half maximum (FWHM) of the $Au4f_{7/2}$ core level was 1.7 eV. The binding energies were referenced to the C1s peak at 284.6 eV due to adventitious carbon. Data processing was performed with the *XPS peak* program, the spectra were decomposed with the least squares fitting routine provided with the software with Gaussian/Lorentzian (90/10) product function. After subtracting a Shirley background, atomic fractions were calculated using peak areas normalized on the basis of sensitivity factors.

The morphologies of the oxides, activated in $H_2$ and after reaction, were recorded by transmission electron microscopy (TEM) with a JEOL 2000 FX microscope, with an acceleration voltage of 200 kV. Specimens for TEM were prepared by ultrasonically dispersing some powder sample in iso-octane and placing a droplet of the suspension on a copper grid covered with a carbon film.

The regeneration capability of the oxide precursors was studied *in situ* by X-ray diffraction experiments using a Siemens D-8 advanced instrument with a Cu Kα radiation (λ = 0.1538 nm) for crystalline phase detection between 10° and 80° ($2\theta$), under

**Table 1**
Chemical analysis of precursor oxides

| Precursors of catalysts | La (wt%) nominal | La (wt%) experimental | Ni (wt%) nominal | Ni (wt%) experimental | Rh (wt%) nominal | Rh (wt%) experimental |
|---|---|---|---|---|---|---|
| $LaNiO_3$-sg | 56.55 | 51.51 | 23.89 | 28.08 | – | – |
| $LaNiO_3$-cp | 56.55 | 51.78 | 23.89 | 27.06 | – | – |
| $LaNi_{0.95}Rh_{0.05}O_3$-sg | 56.08 | 50.73 | 22.49 | 25.83 | 2.07 | 2.72 |
| $LaNi_{0.95}Rh_{0.05}O_3$-cp | 56.08 | 50.79 | 22.49 | 25.74 | 2.07 | 2.80 |

temperature-programmed reduction in 3% $H_2$ (50 mL $min^{-1}$) and temperature-programmed oxidation (TPO) in air (33 mL $min^{-1}$). XRD data were collected while the catalyst was subjected to this reduction/oxidation cycle. Phase identification was carried out by comparison with JCPDF standard spectra software. $LaNiO_3$ perovskite ($2\theta = 32.5^\circ$) and nickel metallic ($2\theta = 44.5^\circ$) crystallite particle sizes were determined by the Scherrer equation using line broadening measurements.

### 2.3. Catalytic measurements

Activity measurements were carried out in a continuous flow, fixed-bed reactor working at atmospheric pressure. 60 mg of the catalyst was placed between quartz glass plugs in the center of a cylindrical tube reactor (11 mm i.d.). The temperatures at the internal and external walls of the reactor were measured by Ni–Cr thermocouples.

Prior to activity measurements, the catalyst precursors were reduced in a 10% $H_2/N_2$ mixture at 700 °C for 2 h, to generate the $Ni^0$ and $Ni^0$–$Rh^0$ metal phases. Subsequently, the reactor was flushed with a nitrogen stream while cooling to room temperature. The reaction was carried out by feeding 3% $CH_4$, diluted with $N_2$ at a total flow of 200 mL $min^{-1}$, WHSV = 200 $h^{-1}$. Stability tests were performed at 450 °C for 5 h. Other reaction conditions were also tested (temperature of 650 °C and total flow of 100 mL $min^{-1}$) for two selected samples, the ones with the highest and the lowest methane conversions. For all cases, the reaction products were analyzed on-line by a Varian 3400 gas-chromatograph provided with thermal conductivity detector and columns packed with Porapak N and 13X molecular sieves. Estimated error of gas-phase composition was within 5%.

In order to understand the relationship between the structural changes of the catalysts precursors and their catalytic performances, a reaction–regeneration–activation–reaction cycle as a function of temperature in the 25–850 °C range was carried out. The activation procedure was the same as described before and it was carried out prior to each reaction cycle. After the reaction, the sample was cooled down to room temperature and exposed to an air flow of 100 mL $min^{-1}$. Then, the sample was heated to 700 °C in 2 h and maintained at this temperature for another 2 h. In addition to these experiments, a series of five activation–reaction–regeneration cycles was performed for the best catalyst. The activation and regeneration procedures were the same as described for the other cycles. However, the stability of the sample was tested at a fixed temperature (450 °C) during 3 h.

## 3. Results and discussion

### 3.1. Chemical analysis and BET specific surface area

Table 1 shows a list of the synthesized perovskite-type oxides and their chemical composition. The values obtained for each element are, within experimental error, very similar to the theoretical ones, indicating a close concurrence between experimental and theoretical molecular formula for the perovskite-type oxides. For all samples, there is a slight excess of nickel, suggesting the presence of another separated phase of nickel (NiO) with the main structure. The results show that both preparation methodologies produce homogeneous structures.

BET specific surface areas of the precursors, calcined in air flow at 750 °C for 5 h, are between 3 and 8 $m^2\ g^{-1}$ (Table 2). These values are rather low and similar to the ones found for similar samples calcined at temperatures in the range of 700–900 °C. These results are in agreement with a previous work [21] that also showed low values of BET areas for these perovskite-type oxides calcined at high temperatures. The specific surface area displayed by these samples mainly corresponds to the external area of the particles approaching a spherical geometry, which is characteristic of non-porous materials. In general, BET specific surface areas were slightly lower for the oxide precursors synthesized by the sol–gel method than for their analogues obtained by co-precipitation. The exception to this trend is the oxide prepared by impregnation of the $La_2O_3$ substrate with the nickel salt, which presented a BET area of 10 $m^2\ g^{-1}$, attributed to the lower calcination temperature (500 °C) used. At a higher calcination temperature (750 °C), the BET area decreased to a value close to that of the $LaNi_{1-x}Rh_xO_3$ ($x = 0$, 0.05) samples. As expected, the change of the specific surface area depends on the grain size and crystal size: the larger the grain size and crystal size, the smaller the specific surface area [22].

### 3.2. Active phase stability study

#### 3.2.1. In situ X-ray diffraction analysis

Table 2 shows the main phases detected by XRD analysis for all the samples: calcined, reduced and the ones used in the catalytic tests. For the calcined samples, the main diffraction lines appeared at 32.8°, 47.0° and 58.0°. These diffraction lines are characteristic of $LaNiO_3$ perovskite (JCPDF 33-0711) rhombohedral structure [23]. Therefore, all samples showed a perovskite structure as the main phase, with high crystalline and well-defined symmetry. In addition to the diffraction lines of the dominant crystalline phase, the tips of a minor NiO phase were also detected, corroborating the

**Table 2**
BET specific surface areas ($m^2\ g^{-1}$), X-ray diffraction analysis and mean nickel particle sizes

| Precursors of catalysts | Specific surface ($m^2\ g^{-1}$) | Main phases (calcined) | Main phases (reduced) | Main phases (after test) | Mean size (calcined) (nm) | Mean size (reduced) (nm) | Mean size (after test) (nm) |
|---|---|---|---|---|---|---|---|
| $LaNiO_3$-sg | 3 | $LaNiO_3$ | $Ni^0$, $La_2O_3$ | $La(OH)_3$, $La_2O_3$, $Ni^0$ | 22 | 21 | 23 |
| $LaNiO_3$-cp | 7 | $LaNiO_3$ | $Ni^0$, $La_2O_3$ | $La(OH)_3$, $La_2O_3$, $Ni^0$, C | 17 | 15 | 31 |
| $LaNi_{0.95}Rh_{0.05}O_3$-sg | 4 | $LaNiO_3$ | $Ni^0$, $La_2O_3$ | $La(OH)_3$, $La_2O_3$, $Ni^0$, C | 16 | 18 | 25 |
| $LaNi_{0.95}Rh_{0.05}O_3$-cp | 8 | $LaNiO_3$ | $Ni^0$, $La_2O_3$ | $La(OH)_3$, $La_2O_3$, $Ni^0$, C | 15 | 13 | 29 |
| $LaNiO_3$-imp | 10 | $LaNiO_3$ | $Ni^0$, $La_2O_3$ | $La(OH)_3$, $La_2O_3$, $Ni^0$, C | 13 | – | 22 |

**Table 3**
*In situ* X-ray diffraction results

| Temperature (°C) | $LaNiO_3$-sg | | $LaNiO_3$-cp | | $LaNi_{0.95}Rh_{0.05}O_3$-sg | | $LaNi_{0.95}Rh_{0.05}O_3$-cp | |
|---|---|---|---|---|---|---|---|---|
| | Phase | Mean size (nm) | Phase | Mean size (nm) | Phase | Mean size (nm) | Phase | Mean size (nm) |
| 25 | $LaNiO_3$ | 19 | $LaNiO_3$ | 17 | $LaNiO_3$ | 16 | $LaNiO_3$ | 15 |
| 200 | $LaNiO_3$ | 20 | $LaNiO_3$ | 19 | $LaNiO_3$ | 18 | $LaNiO_3$ | 16 |
| 400 | $La_2Ni_2O_5$ | 13 | $La_2Ni_2O_5$ | 12 | $La_2Ni_2O_5$ | 9 | $La_2Ni_2O_5$ | 6 |
| | $Ni^0$ | 2 | $Ni^0$ | 2 | $Ni^0$ | 2 | $Ni^0$ | 2 |
| 600 | $La_2O_3$ | 2 | $La_2O_3$ | 4 | $La_2O_3$ | 2 | $La_2O_3$ | 2 |
| | $Ni^0$ | | $Ni^0$ | | $Ni^0$ | | $Ni^0$ | |
| 800 | $La_2O_3$ | 16 | $La_2O_3$ | 12 | $La_2O_3$ | 12 | $La_2O_3$ | 9 |
| | $Ni^0$ | | $Ni^0$ | | $Ni^0$ | | $Ni^0$ | |
| 800 | $La_2O_3$ | 18 | $La_2O_3$ | 11 | $La_2O_3$ | 15 | $La_2O_3$ | 11 |
| | $Ni^0$ | | $Ni^0$ | | $Ni^0$ | | $Ni^0$ | |
| 800 | $La_2O_3$ | 22 | $La_2O_3$ | 14 | $La_2O_3$ | 17 | $La_2O_3$ | 13 |
| | $Ni^0$ | | $Ni^0$ | | $Ni^0$ | | $Ni^0$ | |
| 800 | $La_2O_3$ | 23 | $La_2O_3$ | 15 | $La_2O_3$ | 18 | $La_2O_3$ | 13 |
| | $Ni^0$ | | $Ni^0$ | | $Ni^0$ | | $Ni^0$ | |
| 25 | $La_2O_3$ | 25 | $La_2O_3$ | 17 | $La_2O_3$ | 19 | $La_2O_3$ | 14 |
| | $Ni^0$ | | $Ni^0$ | | $Ni^0$ | | $Ni^0$ | |

results obtained by ICP analyses and indicating that a small fraction of nickel has been segregated to the surface. In the substituted $LaNi_{0.95}Rh_{0.05}O_3$ samples, neither changes in the diffraction lines of the perovskite phase nor the appearance of new lines relative to crystalline $Rh_2O_3$ were observed. It is interesting to point out that even the precursor synthesized by impregnation exhibits the characteristic diffraction lines of the $LaNiO_3$ perovskite structure. This observation indicates that during air calcining, a solid-state reaction occurs between the NiO particles deposited on the surface and the topmost layers of $La_2O_3$ particles, yielding the $LaNiO_3$ perovskite structure. By applying the Scherrer equation to the most intense diffraction lines in the XRD patterns [24], the average values of crystallite sizes were calculated for the calcined, reduced and used samples. In these calculations, the most intense reflection of the perovskite phase at 32.8° was selected for the calcined samples, whereas for $Ni^0$, the reflection chosen was at 44.5° for the reduced samples. Table 2 compiles the main crystalline phases and average crystallite sizes for all samples. Nickel crystallite sizes of calcined samples are in the 15–22 nm range, being somewhat larger for the $LaNiO_3$-sg sample. In addition, $Ni^0$ crystallite sizes in the reduced samples showed the same trend observed for the calcined counterparts, indicating that there is not an accentuated sintering of metal particles during $H_2$-reduction (cf. Table 2). Comparing Rh-containing samples with the equivalent catalysts without Rh, one can notice that the addition of the noble metal reduced the nickel crystallite sizes for all tested conditions (calcined and reduced, regardless of the temperature), in agreement with a previously reported work [25].

XRD patterns of the used samples (not shown) showed one peak at 44.4°, indexed to $Ni^0$ (JCDF 0031043) and peaks indexed to $La(OH)_3$ and $La_2O_3$ species. $Ni^0$ crystallite sizes of the used catalysts increased as compared to that of the perovskite-type precursor (Table 2), with the exception of the $LaNiO_3$-sg sample, which remained virtually unchanged. The increase observed in crystallite size was more accentuated for co-precipitated catalysts ($LaNiO_3$-cp and $LaNi_{0.95}Rh_{0.06}O_3$-cp) than for those synthesized by the sol–gel method. Consequently, when subjected to the reaction environment, sintering and growth of Ni particles appear to be inhibited in samples synthesized by the sol–gel method [26]. Peaks of graphitic carbon were observed in all catalytic test samples with similar intensities. As expected, the intensities of these peaks were larger for the samples tested at 650 °C.

*In situ* XRD analyses were performed during a reduction–oxidation–reduction cycle for all the samples. The diffraction patterns were recorded at different temperatures and a list of the main phases, detected as a function of reduction temperature, is shown in Table 3. As it can be seen, samples synthesized by co-precipitation showed smaller nickel crystallite sizes, which decrease with the addition of rhodium. As an example, these diffraction patterns are shown in Fig. 1 for the $LaNi_{0.95}Rh_{0.05}O_3$-cp. $Ni^{3+}$ cations become reduced to metal ($Ni^0$) during the first reduction, whereas lanthanum forms its respective oxide ($La_2O_3$) upon increasing the reduction temperature. All diffraction patterns show a phase change around 400 °C, which is attributed to the reduction of the $LaNiO_3$ phase into a brownmillerite intermediate structure $La_2Ni_2O_5$, in which nickel ions are in the oxidation state Ni(II) [27]. At temperatures above 600 °C, the crystal structure collapses, with the subsequent formation of $Ni^0$ crystallites deposited on the $La_2O_3$, in agreement with previously reported works. For the re-oxidized samples, the XRD results indicate that the catalysts can reversibly interchange between a perovskite-type structure and nickel nanoparticles supported on $La_2O_3$, throughout the oxidation, reduction and re-oxidation cycle. Under reducing conditions, the metal emerges from the framework of the perovskite to form metallic clusters or nanoparticles. Under oxidative conditions, the metal re-enters the framework to refresh itself. Through these experiments, it was confirmed that nickel can move back and forth between the B-site in the perovskite structure and the metallic nanoparticles, responding to the inherent cycling between an oxidative and a reductive environment. In addition, we observed a small increase of the nickel crystallite size after the redox cycles, for all samples.

### 3.2.2. Temperature-programmed reduction

Fig. 2 displays TPR profiles of $LaNi_{1-x}Rh_xO_3$ samples and of $Ni/La_2O_3$. The profile corresponding to the impregnated sample (curve A) exhibits two main peaks around 340 and 470 °C. According to *in situ* XRD data, the lower temperature peak is usually attributed to the reduction of $Ni^{3+}$ into $Ni^{2+}$ and to the formation of a $La_2Ni_2O_5$ phase. On the other hand, the higher temperature peak can be associated to the reduction of the brownmillerite $La_2Ni_2O_5$ phase to $Ni^0$ and $La_2O_3$, which is also consistent with *in situ* XRD profiles previously presented. Generally, the reduction of perovskite-type oxides leads to metallic nickel particles dispersed on $La_2O_3$ [15].

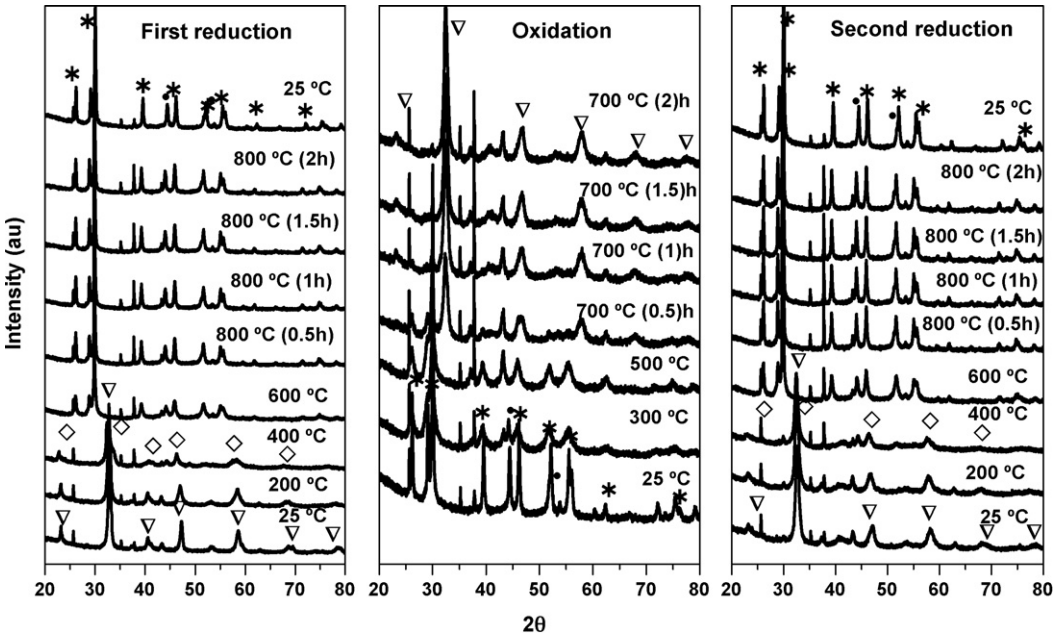


**Fig. 1.** *In situ* XRD of $LaNi_{0.95}Rh_{0.05}O_3$-cp as synthesized, reduced and oxidized at different temperatures: (▽) $LaNiO_3$; (●) $Ni^0$; (∗) $La_2O_3$; (◊) $La_2Ni_2O_5$.

Profiles (B) and (C) are relative to the reduction patterns of $LaNiO_3$ prepared by the sol–gel and the co-precipitation methods, respectively. These profiles exhibit two major $H_2$ consumption peaks, like the ones observed for the impregnated sample. However, these peaks are shifted around 40 °C to higher reduction temperature. Since the major phase detected by XRD for all these samples was $LaNiO_3$, this difference in the reduction temperature is probably due to the differences observed in the BET area. Since the reduction process of these oxides is usually diffusion, controlled by water molecules moving from the inner layers to the surface of the material, smaller particles are easily reduced. It has already been pointed out that the specific surface area of all samples is mainly due to the external surface of the particles, with the impregnated sample presenting the highest BET area. Therefore, it is expected that $LaNiO_3$ oxides synthesized by co-precipitation and by sol–gel methods would be more difficult to reduce, since they have smaller BET areas. Besides, the two major $H_2$-consumption peaks, the previously discussed B and C profiles, also showed a shoulder at lower temperature, around 290 °C, which could be associated to the reduction of a small amount of a segregated nickel oxide phase, as observed by the XRD analysis.

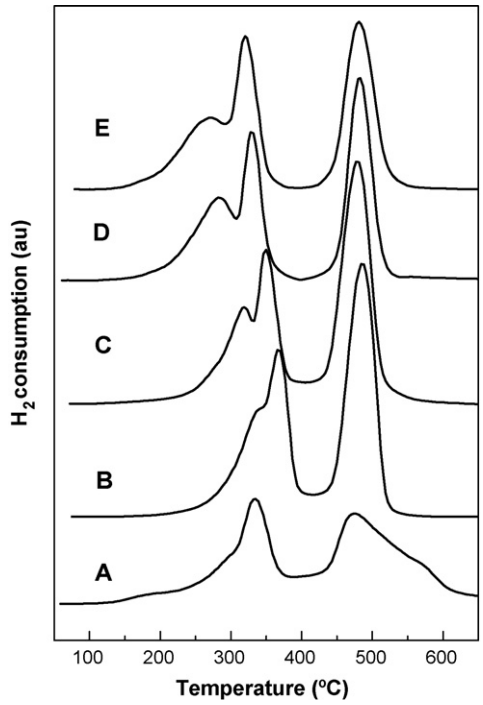


**Fig. 2.** Temperature-programmed reduction profiles of oxide precursors: (A) $LaNiO_3$-imp; (B) $LaNiO_3$-sg; (C) $LaNiO_3$-cp; (D) $LaNi_{0.95}Rh_{0.05}O_3$-sg; (E) $LaNi_{0.95}Rh_{0.05}O_3$-cp.

The addition of rhodium to the perovskite-type oxides did not have a strong effect on the reduction profiles of these materials. The only difference is that the main peaks appear shifted by ca. 20 °C toward lower reduction temperatures. As rhodium is reduced at lower temperatures than $Ni^{3+}$ and $Ni^{2+}$, the generated Rh atoms can increase the reducibility of the cationic nickel via spillover of H-atoms [22].

### 3.3. Surface composition for calcined and activated oxide precursors

The chemical state of the elements and the surface composition of the calcined and activated samples of $LaNi_{1-x}Rh_xO_3$ oxides were determined by X-ray photoelectron spectroscopy. The binding energies of O 1s, C 1s, Ni $2p_{1/2}$, La $3d_{5/2}$ and Rh $3d_{5/2}$ core-levels of calcined $LaNi_{1-x}Rh_xO_3$ are presented in Table 4. Ni 2p signals are complex because of the overlapping of the Ni $2p_{3/2}$ and La $3d_{3/2}$ signals, which conceals both an accurate measurement of nickel binding energy as well as its intensity. In order to be able to analyze the nickel data, the less intense Ni $2p_{1/2}$ component of the Ni 2p doublet was selected for binding energy measurements and quantification. According to the literature, the most intense feature of Ni $2p_{3/2}$ around 855 eV arises from $Ni^{2+}/Ni^{3+}$ ions surrounded by oxide ions [28]. The Ni $2p_{1/2}$ binding energies at 872.9–873.1 eV (Table 4) point to the presence of ionic nickel species. Due to the close similarity of binding energies of $Ni^{2+}$ and $Ni^{3+}$, it is difficult, if not impossible, to discriminate between both species by

**Table 4**
Binding energy (eV) of core electrons of LaNi perovskite samples

| | La $3d_{5/2}$ | Ni $2p_{1/2}$ | C 1s | O 1s | Rh $3d_{5/2}$ |
|---|---|---|---|---|---|
| Calcined samples | | | | | |
| $LaNiO_3$-sg | 834.0 | 873.0 | – | 528.6 (32), 530.7(41), 532.0 (28) | – |
| $LaNiO_3$-cp | 834.3 | 873.0 | – | 528.8 (36), 530.7 (35), 532.0 (29) | – |
| $LaNi_{0.95}Rh_{0.05}O_3$-sg | 834.1 | 873.3 | – | 528.9 (32), 530.9 (40), 532.4 (28) | 309.2 |
| $LaNi_{0.95}Rh_{0.05}O_3$-cp | 833.6 | 872.5 | – | 528.4 (34), 530.2 (37), 531.5(29) | 308.8 |
| Samples after activation | | | | | |
| $LaNiO_3$-sg | 834.1 | 872.1 | – | 529.1, 531.3 | – |
| $LaNiO_3$-cp | 834.2 | 871.5 | – | 529.8, 531.2 | – |
| $LaNi_{0.95}Rh_{0.05}O_3$-sg | 834.2 | 871.8 | – | 529.0, 531.2 | 307.1 |
| $LaNi_{0.95}Rh_{0.05}O_3$-cp | 834.6 | 872.0 | – | 529.7, 531.4 | 307.2 |
| $LaNiO_3$-imp | 833.7 | 870.6 | – | 528.7, 530.3, 531.5 | – |

photoelectron spectroscopy alone. However, the observation of a satellite line, which is the fingerprint of $Ni^{2+}$ ions, can be taken as conclusive for the presence of an important proportion of $Ni^{2+}$ on the surface. The La $3d_{5/2}$ and La $3d_{3/2}$ signals, split by 4.3 eV in two components, which have been assigned to the transfer of an oxygen-centered electron to the empty 4f shell accompanying the ionization process [29]. The corresponding binding energies of La $3d_{5/2}$ peak at 834.5–834.7 eV (Table 4) are lower than those measured for $La(OH)_3$ and similar to those of $La_2O_3$ [30]. However, the low resolution of the two La $3d_{5/2}$ peak components suggests the presence of other species such as $La_2O_2CO_3$ and/or $La(OH)_3$ [31]. The chemical state of oxygen on the surface was also examined. The O 1s spectra of all samples are showed in Fig. 3, showing three components at: (i) 528.4–528.9 eV; (ii) 530.2–530.9 eV; (iii) 531.5–532.4 eV. Type (i) peak is usually ascribed to weakly bonded oxygen ($O^{2-}$), while types (ii) and (iii) components may arise from lattice oxygen and hydroxyl/carbonate groups, respectively [32,33]. The C 1s core-level (Fig. 4) showed two components at 284.9 and 285.6 eV due to CC/CH and C—O bonds of carbon contamination, respectively, and a third one at 289.2–289.4 eV, which is characteristic of carbonate species. These carbonate structures are developed in La-based perovskite-type oxides as a consequence of carbonation of the basic $La^{3+}$ cations, when exposed to room atmosphere. For the two calcined $LaNi_{0.95}Rh_{0.05}O_3$ samples (Fig. 5), the binding energy of the Rh $3d_{5/2}$ signal appeared at 308.8–309.2 eV, which is typical of $Rh^{3+}$ ions surrounded by oxide anions [34]. For the reduced samples, there is a shift of the binding energies of the Rh $3d_{5/2}$ signal to 307.1–307.2 eV, indicating the presence of metallic rhodium on the surface.

Quantification of the Ni/La and Rh/La surface atomic ratios for calcined and activated samples are summarized in Table 5, calculated from the intensities of the La $3d_{5/2}$, Ni $2p_{1/2}$ and Rh $3d_{5/2}$ signals, with atomic sensitivity factors given by Wagner et al. [35]. It can be noted that the Ni/La ratios for the calcined samples are

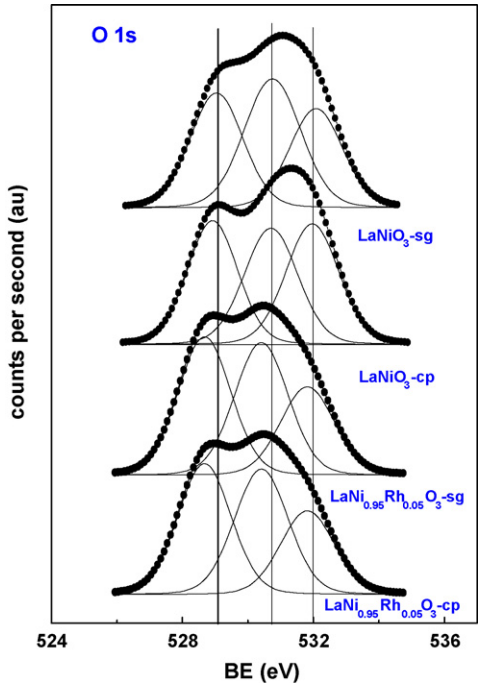


**Fig. 3.** Phoelectron spectra of the O 1s core-level of oxide precursors: $LaNiO_3$-sg, $LaNiO_3$-cp, $LaNi_{0.95}Rh_{0.05}O_3$-sg and $LaNi_{0.95}Rh_{0.05}O_3$-cp.

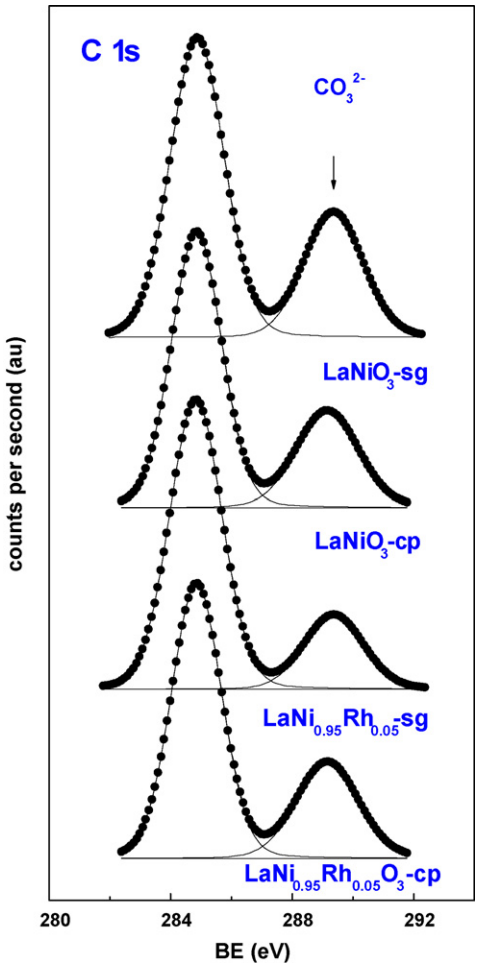


**Fig. 4.** Phoelectron spectra of the C 1s core-level of oxide precursors: $LaNiO_3$-sg, $LaNiO_3$-cp, $LaNi_{0.95}Rh_{0.05}O_3$-sg and $LaNi_{0.95}Rh_{0.05}O_3$-cp.

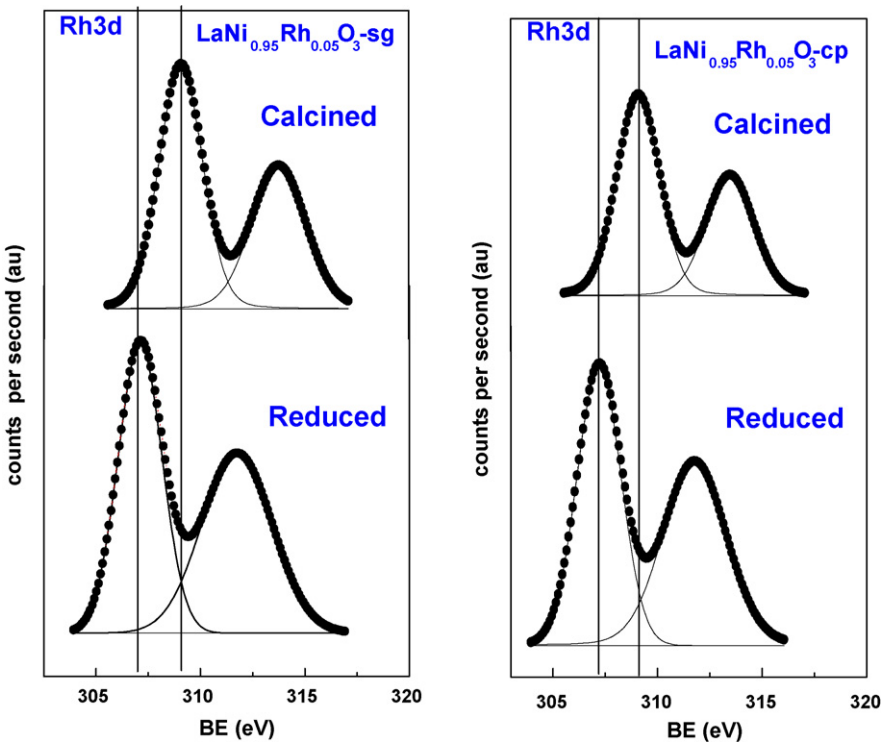


**Fig. 5.** Phoelectron spectra of the Rh 3d core-level of the activated solids: $LaNi_{0.95}Rh_{0.05}O_3$-sg and $LaNi_{0.95}Rh_{0.05}O_3$-cp.

slightly higher than the expected theoretical values derived from the composition for both the $LaNiO_3$ and $LaNi_{0.95}Rh_{0.05}O_3$ samples. The Ni-enrichment observed in the $LaNiO_3$ samples agrees with ICP, X-ray diffraction and TPR profiles, which showed the presence of a minor, separate NiO phase deposited on the $LaNiO_3$ substrate. In addition, surface $La^{3+}$ cations of the perovskite-type phase are partly carbonated, as judging from the high $CO_3^{2-}$/La surface ratios (Table 5). The concentration of surface carbonates decreased slightly in the $LaNi_{0.95}Rh_{0.05}O_3$ samples. On the other hand, the Rh/La surface atomic ratios were higher than the nominal values. This fact suggests the presence of a rhodium oxide phase, produced from Rh runoff from the perovskite-type structure during catalyst synthesis. For the activated samples, it is important to point out that the Ni/La ratios increased for all solids, indicating that there is an enrichment of the surface with nickel. This effect was more evident for the rhodium-containing catalysts, especially for $LaNi_{0.95}Rh_{0.05}O_3$-cp. Therefore, the presence of rhodium increases the amount of nickel on the surface. This result about promotion function of the noble metals has already been reported in the literature [36].

### 3.4. Transmission electron microscopy

TEM images of the $LaNi_{1-x}Rh_xO_3$ catalysts, both activated and after 5 h on-stream, are displayed in Fig. 6. The images, obtained for the reduced samples, show that, in general, catalysts synthesized by co-precipitation produced smaller nickel particle than those obtained by the sol–gel method, which is in agreement with the XRD results. Usually, the metallic nickel particles are spherical, with sizes between 10 and 25 nm. The reduced and the used catalysts presented opposite trends regarding the particle sizes, as shown by TEM images. As observed by XRD analyses, TEM results showed that nickel particles sintered more during catalytic tests for samples prepared by co-precipitation than the counterparts obtained by sol–gel. Another feature detected for the used samples is the presence of nanotube-type carbon deposits. This is in agreement with previous reports in the literature [37], which also show that the presence of metallic nickel, with particle sizes within the range obtained in this work(?) favors the formation of filamentous carbon deposits. The diameters of the nanotubes were similar to that of their precursor nickel counterpart, being narrower for the samples synthesized by the sol–gel method than those obtained by co-precipitation. In addition, TEM images of used samples show that these nanotubes are multi-walled, which is also consistent with the range of nickel particle sizes observed. Similarly, Ermakova et al., when decomposing methane on nickel catalysts, reported the formation of multi-walled carbon nanotubes [5].

**Table 5**
Surface atomic ratios of LaNi perovskite samples

| Samples | Calcined | | | After activation | |
|---|---|---|---|---|---|
| | Ni/La at | Rh/La at | $CO_3^{2-}$/La at | Ni/La at | Rh/La at |
| $LaNiO_3$-sg | 1.200 | – | 0.701 | 1.290 | – |
| $LaNiO_3$-cp | 1.231 | – | 0.782 | 1.483 | – |
| $LaNi_{0.95}Rh_{0.05}O_3$-sg | 1.320 | 0.101 | 0.604 | 1.540 | 0.092 |
| $LaNi_{0.95}Rh_{0.05}O_3$-cp | 1.090 | 0.106 | 0.576 | 1.960 | 0.104 |
| $LaNiO_3$-imp | – | – | – | 1.021 | – |

### 3.5. Catalytic activity

Methane conversion as a function of time measured at 450 °C is presented in Fig. 7. Being far from thermodynamic constraints, results at this temperature allow the comparison of catalysts performances. No methane decomposition products other than hydrogen were detected in the effluent gas during the experiments. Thus, deposited carbon and hydrogen can be regarded as the only products of methane decomposition. At the experimental conditions used, all catalysts show activity in the methane decomposition process, with methane conversions ranging between 14% and 28%.

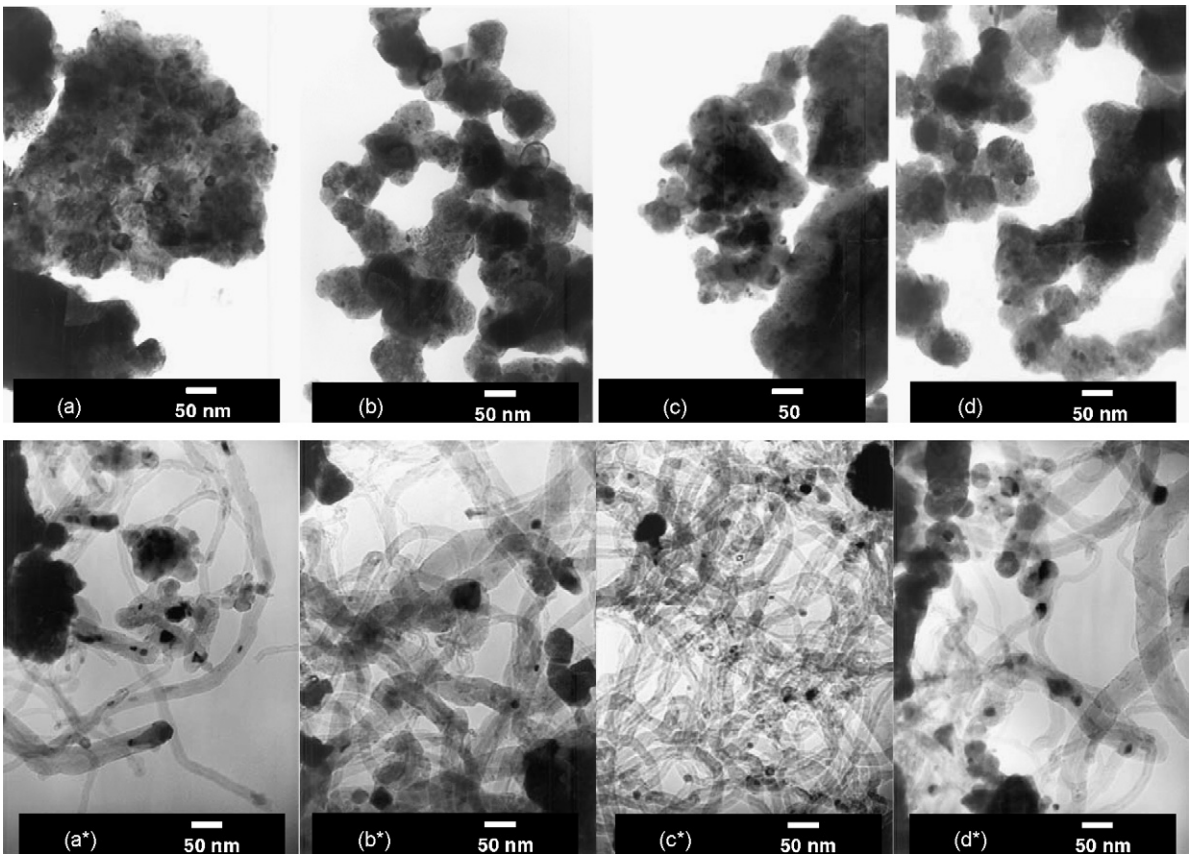


**Fig. 6.** TEM images of the activated materials and after 5 h on stream: (a) $LaNiO_3$-sg; (b) $LaNiO_3$-cp; (c) $LaNi_{0.95}Rh_{0.05}O_3$-sg; (d) $LaNi_{0.95}Rh_{0.05}O_3$-cp.

The catalytic activities decrease only slightly with time for all the studied solids, in spite of the increasing concentration of carbon deposited on the catalysts during the tests. The mechanism for CDM includes steps to dissociate methane, generating adsorbed hydrogen atoms and carbon on the surface [13,38,39]. Subsequently, there is the diffusion of carbon through the nickel particle and the precipitation of this carbon on the support side, forming the nanotubes. It is also possible that carbon deposits end up encapsulating the nickel particles, which leads to catalyst deactivation. The surface equations of this mechanism, according to Chen et al. [39], are listed below:

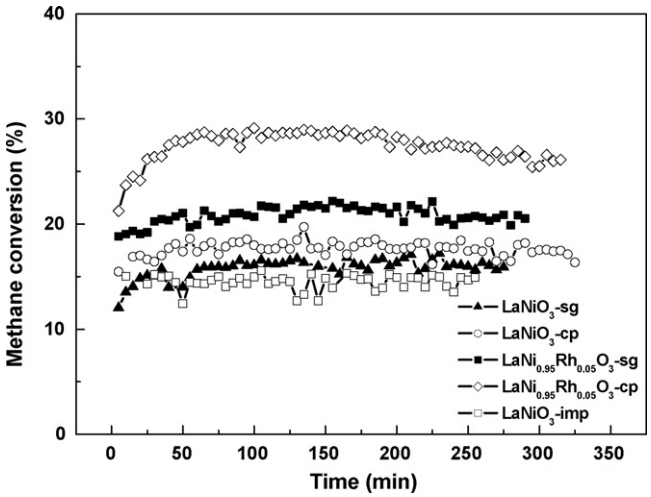


**Fig. 7.** $CH_4$ conversions as a function of time on stream at 450 °C for catalysts derived from: (□) $LaNiO_3$-imp; (▲) $LaNiO_3$-sg; (○) $LaNiO_3$-cp; (■) $LaNi_{0.95}Rh_{0.05}O_3$-sg; (◊) $LaNi_{0.95}Rh_{0.05}O_3$-cp precursors. WHSV = 200 $h^{-1}$, $CH_4$ = 3%.

Methane dissociation

$$CH_4 + 2S \leftrightarrows CH_3\text{-}S + H\text{-}S$$

$$CH_3\text{-}S + S \leftrightarrows CH_2\text{-}S + H\text{-}S$$

$$CH_2\text{-}S + S \leftrightarrows CH\text{-}S + H\text{-}S$$

$$CH\text{-}S + S \leftrightarrows C\text{-}S + H\text{-}S$$

Hydrogen desorption

$$2H\text{-}S \leftrightarrows H_2 + 2S$$

Carbon dissolution/segregation

$$C\text{-}S \leftrightarrows C_{Ni,f} + S$$

Carbon diffusion through the nickel particle

$$C_{Ni,f} \leftrightarrows C_{Ni,r}$$

Carbon dissolution/precipitation

$C_{Ni,r} \leftrightarrows C_f$

Encapsulation carbon formation

$nC\text{-}S \leftrightarrows C_{enc}$

where S is an adsorption site, $C_{Ni,f}$ represents the carbon dissolved in the front part of a nickel particle, $C_{Ni,r}$ represents the carbon dissolved in the portion of the nickel particle in contact with the support and $C_{enc}$ represents the carbon that encapsulates the nickel particles, which leads to the catalyst deactivation.

The fact that the catalysts maintain their activities even after massive carbon deposition indicates that these deposits are of the nanotube-type. In addition, the reaction occurs in a way that a crystal face of the nickel or rhodium particle is always clean enough to expose sufficient active sites to make the catalytic process continue.

The highest methane conversion values were achieved by the catalyst obtained from $LaNi_{0.95}Rh_{0.05}O_3$ synthesized by co-precipitation. This behavior could be explained by the formation of highly dispersed Rh clusters, which remain on the perovskite-type and/or $La_2O_3$ substrate during on-stream operation. XPS results of activated precursors showed that $LaNi_{0.95}Rh_{0.05}O_3$ synthesized by co-precipitation had a higher Ni/La ratio. This confirms that nickel dispersion is favored by the addition of rhodium. TPR analysis also showed that the presence of Rh increases the reducibility of $Ni^{3+}/Ni^{2+}$ cations from the perovskite-type oxides, producing a higher concentration of the active phase on the surface of the support. In general, a relationship seems to exist among specific surface area, particle size and catalytic behavior in the reaction.

In order to observe how the performances of these catalysts were affected by the reaction temperature, the same catalytic tests were performed at 650 °C using $LaNi_{0.95}Rh_{0.05}O_3$-cp and $LaNiO_3$-sg. The results are shown in Fig. 8. As expected, $LaNi_{0.95}Rh_{0.05}O_3$-cp exhibited a better performance, around 50% of methane conversion, when compared to $LaNiO_3$-sg (around 20–30%). However, for $LaNi_{0.95}Rh_{0.05}O_3$-cp, the test had to be interrupted after 100 min due to pressure rise in the reactor, caused by massive carbon deposits. Both samples deactivated slowly with time. This effect of stronger catalyst deactivation during methane decomposition while using higher reaction temperature was previously reported in the literature by Villacampa et al. [13] and Chen et al. [39]. According to these authors, this happens because of an imbalance between the rates of carbon deposition and nanotube formation, which causes encapsulating of the active particles.

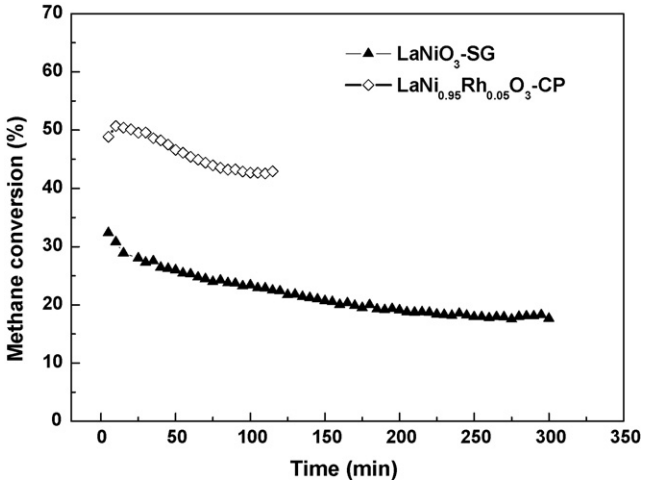


**Fig. 8.** $CH_4$ conversions as a function of time on stream at 650 °C for catalysts derived from: (▲) $LaNiO_3$-sg; (◊) $LaNi_{0.95}Rh_{0.05}O_3$-cp precursors. WHSV = 100 $h^{-1}$, $CH_4$ = 3%.

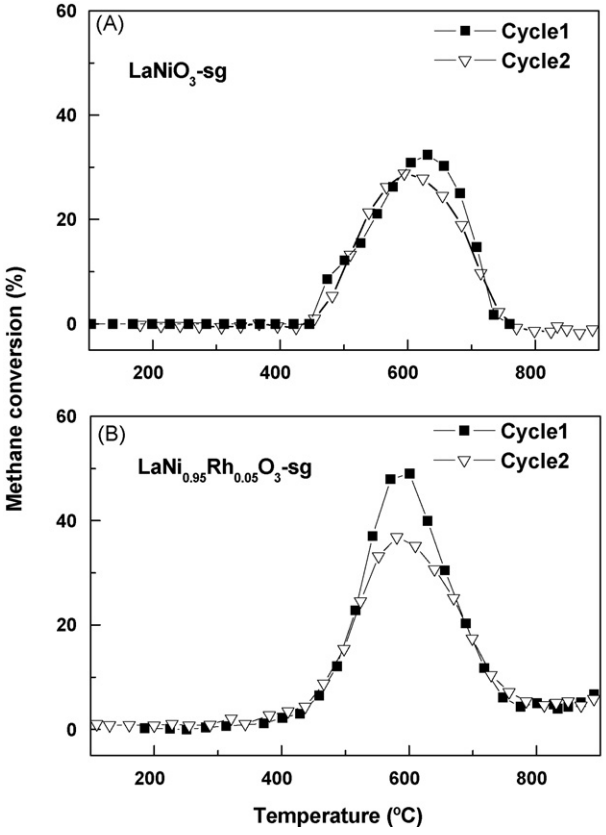


**Fig. 9.** $CH_4$ conversions as a function of temperature during two consecutive activation–reaction–oxidation cycles. (A) $LaNiO_3$-sg; (B) $LaNi_{0.95}Rh_{0.05}O_3$-cp precursors. WHSV = 200 $h^{-1}$, $CH_4$ = 3%.

In addition to these catalytic tests performed at higher temperature, we also used the same catalysts to probe the regeneration capabilities by doing a reaction–regeneration–activation–reaction cycle as a function of reaction temperature. The results presented in Fig. 9 show that the activity of both samples was very similar during the first and second reaction cycle. There was only a small loss of activity for both samples, which could be explained by *in situ* XRD results. As these data demonstrated, when the sample is submitted to the oxidation (regeneration) cycle, the perovskite-type structure is regenerated. This structure helps to avoid the sintering of the nickel particles that is so common during reduction–oxidation cycles.

In order to confirm the regeneration capabilities of this perovskite-like type structures, we also conducted a series of 5 activation–reaction–regeneration cycles at 450 °C for $LaNi_{0.95}Rh_{0.05}O_3$-cp. The data are presented in Fig. 10. Each reaction cycle lasted 3 h. Methane conversion was maintained stable even after several cycles of activation, reaction and regeneration. Again, this result agrees well with *in situ* XRD data and with the other regeneration cycles performed before. In addition, thermal gravimetric analysis data also show that the regeneration procedure is able to remove all carbon deposits on the catalyst surface. Therefore, it can be said that during the oxidation treatment, nickel particles are free of carbon deposits and can migrate back to the perovskite-like structure as shown by XRD data. The fact that this structure is regenerated avoids the sintering of nickel particles and maintains the catalyst activity.

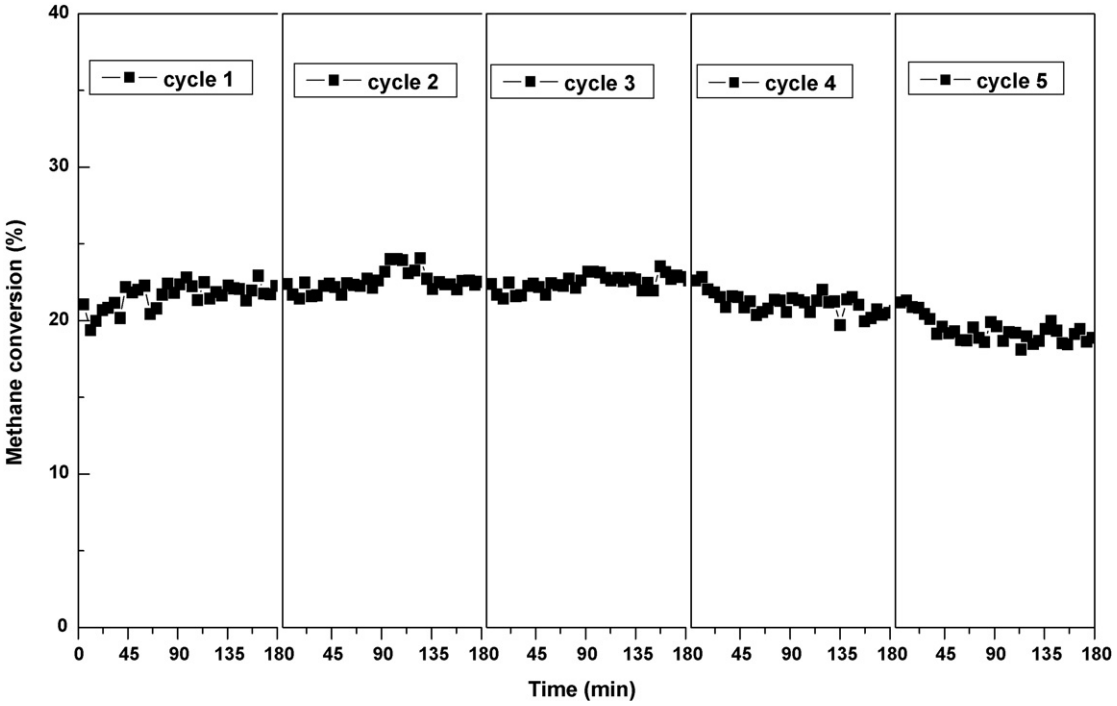


**Fig. 10.** $CH_4$ conversions as a function of time on stream during five consecutive activation–reaction–oxidation cycles using the $LaNi_{0.95}Rh_{0.05}O_3$-cp sample. Reaction temperature = 450 °C, WHSV = 200 $h^{-1}$ and $CH_4$ = 3%.

## 4. Conclusions

All synthesized samples showed a perovskite structure as the main phase, with high stability even when subjected to reduction–oxidation–reduction cycles.

$LaNiO_3$ reduce to a brownmillerite intermediate $La_2Ni_2O_5$ structure, which collapses through the formation of $Ni^0$ crystallites deposited on the $La_2O_3$. On the Rh-loaded perovskites, highly dispersed Rh clusters are formed and remain on the perovskite-type and/or $La_2O_3$ substrate during on-stream operation, confirming that nickel dispersion is favored by the addition of rhodium. TPR analysis also showed that the presence of Rh increases the reducibility of $Ni^{3+}/Ni^{2+}$ cations from the perovskite-type oxides, producing a higher concentration of the active phase on the surface of the support. A relationship among specific surface area, particle size and catalytic behavior in the reaction is invoked. Under oxidative conditions, the perovskite system becomes reversible with nickel re-entering the $LaNiO_3$ framework structure accounting for the regenerative capability of these solids.

At reaction temperatures as low as 450 °C, methane was decomposed into carbon and $H_2$, with $LaNi_{0.95}Rh_{0.05}O_3$ synthesized by co-precipitation being the most active catalyst. All catalysts maintained sustained activity even after massive carbon deposition, indicating that these deposits are of the nanotube-type. The reaction seems to occur in a way that a nickel or rhodium crystal face is always clean enough to expose sufficient active sites to make the catalytic process continue.

## Acknowledgements

MER gratefully acknowledges financial support for a doctoral fellowship (I3P-program) from the European Social Fund. CEH appreciatively recognizes the postdoctoral fellowship from the Brazilian agency CNPq (#210271-2006/0). Financial support from MEC, Spain (Project ENE2004-07345-C03-01/ALT) is also acknowledged.

## References

[1] T.V. Chouldhary, C. Sivadinarayana, C.C. Chusuei, A. Klinghoffer, D.W. Goodman, J. Catal. 199 (2001) 9–18.
[2] Z. Bai, H. Chen, B. Li, W. Li, Int. J. Hydrogen Energy 32 (1) (2007) 32.
[3] N. Muradov, F. Smith, A. T-Raissi, Catal. Today 102–103 (2005) 165.
[4] K. Otsuka, S. Takenama, H. Ohtsuki, Appl. Catal. A 273 (2004) 113.
[5] M.A. Ermakova, D.Y. Ermakov, G.G. Krushinov, L.M. Plyasova, J. Catal. 187 (1999) 77.
[6] S. Takenaka, S. Kobayashi, H. Ogihara, K. Otsuka, J. Catal. 217 (1) (2003) 79–87.
[7] T. Choudhary, E. Aksoylu, D.W. Goodman, Catal. Rev. Sci. Eng. 45 (2003) 151.
[8] K.P. Jong, J.W. Geus, Catal. Rev. Sci. Eng. 42 (4) (2000) 481.
[9] R.A. Couttenye, M.H. De Vila, S.L. Suib, J. Catal. 233 (2) (2005) 317.
[10] Y. Li, B. Zhang, X. Xie, J. Liu, Y. Xu, W. Shen, J. Catal. 235 (2) (2006) 412.
[11] J. Ashok, S. Naveen Kumar, A. Venugopal, V. Durga Kumari, M. Subrahmanyam, J. Power Sources 164 (2007) 809.
[12] G. Bonura, O. Di Blasi, L. Spadaro, F. Arena, F. Frusteri, Catal. Today 116 (2006) 298.
[13] J.I. Villacampa, C. Royo, E. Romeo, J.A. Montoya, P. Del Angel, A. Monzón, Appl. Catal. A 252 (2003) 363.
[14] F.J. Spiess, S.L. Suib, K. Irie, Y. Hayashi, H. Matsumoto, Catal. Today 89 (1/2) (2004) 35.
[15] M.R. Goldwasser, M.E. Rivas, E. Pietri, M.J. Pérez-Zurita, M.L. Cubeiro, A. Griboval-Constant, G. Leclercq, J. Mol. Catal. A 228 (2005) 325.
[16] G. Valderrama, M.R. Goldwasser, C. Urbina, J.M. Tatibouët, J. Barrault, C. Batiot-Dupeyrat, F. Martínez, Catal. Today 107 (2005) 785.
[17] F. Basile, G. Fornasari, F. Trifirò, A. Vaccari, Catal. Today 77 (2002) 215.
[18] A.K. Norman, M.A. Morris, J. Mater. Process. Technol. 92–93 (1999) 91; M. Kuras, R. Roucou, C. Petit, J. Mol. Catal. A 265 (2007) 209.
[19] M.P. Pechini, US Patent 3 (1967) 330.
[20] F. Simonot, G. Gain, G. Maire, Appl. Catal. B 11 (1997) 167.
[21] M. Bradford, M.A. Vannice, J. Catal. 183 (1999) 69.
[22] R. Tan, Y. Zhu, J. Feng, S. Ji, L. Cao, J. Alloys Compd. 337 (2002) 282.
[23] G. Sierra, F. Mondragón, J. Barrault, J.M. Tatibouët, C. Batiot-Dupeyrat, Appl. Catal. A 311 (2006) 164.
[24] H.P. Klug, L.E. Alexander, X-ray Diffraction Procedures for Polycrystalline and Amorphous Materials, Wiley, London, 1962.
[25] J.A.C. Dias, J.M. Assaf, J. Power Sources 136 (2004) 106.
[26] C. Batiot-Dupeyrat, G. Valderrama, A. Meneses, F. Martínez, J. Barrault, J.M. Tatibouet, Appl. Catal. A 248 (2003) 143.
[27] S.M. Lima, J.M. Assaf, M.A. Peña, J.L.G. Fierro, Appl. Catal. A 331 (2006) 94.
[28] D. Briggs, M.P. Seah (Eds.), Practical Surface Analysis by Auger and X-ray Photoelectron Spectroscopy, 2nd ed., Wiley, Chichester, 1990.
[29] L.P. Haack, C.R. Peters, J.E. Vriesand, K. Otto, Appl. Catal. A 87 (1992) 103.
[30] J.S. Ledford, M. Houalla, A. Proctor, D.M. Hercules, J. Phys. Chem. 93 (1989) 6770.

[31] M.A. Peña, J.L.G. Fierro, Chem. Rev. 101 (2001) 1981.
[32] J.L.G. Fierro, Catal. Today 8 (1990) 153.
[33] H.J. Gysling, J.R. Monnier, G. Apai, J. Catal. 103 (1987) 407.
[34] R.M. García de la Cruz, H. Falcón, M.A. Peña, J.L.G. Fierro, Appl. Catal. B 33 (2001) 45.
[35] C.D. Wagner, L.E. Davis, M.V. Zeller, J.A. Taylor, R.H. Raymond, L.H. Gale, Surf. Interface Anal. 3 (1981) 211.
[36] Y. Mukainakano, L. Baitao, S. Kado, T. Miyazagua, K. Okumura, T. Miyao, S. Naito, K. Kunimori, K. Tomishigue, Appl. Catal. A 318 (2007) 252.
[37] B. Pawelec, S. Damyanova, K. Arishtirova, J.L.G. Fierro, L. Petrov, Appl. Catal. A 323 (2007) 188.
[38] C. He, N. Zao, C. Shi, X. Du, J. Li, Mater. Chem. Phys. 97 (2005) 109.
[39] D. Chen, K.O. Christensen, E. Ochoa-Fernandez, Z. Yu, B. Totdal, N. Latone, A. Mozon, A. Holmen, J. Catal. 229 (2005) 82.